Modeling of microbial kinetics and mass transfer in bioreactors simulating the natural attenuation of arsenic and iron in acid mine drainage

Maria Garcia-Rios, Laurent de Windt, Linda Luquot, Corinne Casiot

▶ **To cite this version:**

Maria Garcia-Rios, Laurent de Windt, Linda Luquot, Corinne Casiot. Modeling of microbial kinetics and mass transfer in bioreactors simulating the natural attenuation of arsenic and iron in acid mine drainage. Journal of Hazardous Materials, 2021, 405, pp.124133. 10.1016/j.jhazmat.2020.124133 . hal-03012675

HAL Id: hal-03012675
https://hal.science/hal-03012675

Submitted on 24 Nov 2020

HAL is a multi-disciplinary open access archive for the deposit and dissemination of scientific research documents, whether they are published or not. The documents may come from teaching and research institutions in France or abroad, or from public or private research centers.

L'archive ouverte pluridisciplinaire **HAL**, est destinée au dépôt et à la diffusion de documents scientifiques de niveau recherche, publiés ou non, émanant des établissements d'enseignement et de recherche français ou étrangers, des laboratoires publics ou privés.

Modeling of microbial kinetics and mass transfer in bioreactors simulating the natural attenuation of arsenic and iron in acid mine drainage

Maria Garcia-Rios [a], Laurent De Windt [b], Linda Luquot [c], Corinne Casiot [a,*]

a HydroSciences Montpellier, University of Montpellier-CNRS-IRD, Montpellier (France)

b Centre de Geosciences, MINES ParisTech, PSL University, Fontainebleau (France)

c Géosciences Montpellier, Université Montpellier, CNRS, Montpellier (France)

* Corresponding author: corinne.casiot-marouani@umontpellier.fr.
Address : Université de Montpellier, HydroSciences - CC57, 163 rue Auguste Broussonnet, 34090 Montpellier, France. Telephone : +33(0)467143356 ; fax : +33(0)467144774

Abstract.

Natural attenuation in acid mine drainage (AMD) due to biological iron and arsenic oxidation offers a promising strategy to treat As-rich AMD in passive bioreactors. A reactive transport model was developed in order to identify the main controlling factors. It simulated batch and flow-through experiments that reproduced natural attenuation in a high-As AMD. The 2-D model coupled second-order microbial kinetics (Fe- and As- oxidation) and geochemical reactions to hydrodynamic transport. Oxidation only occurred in the biofilm with an oxygen transfer from the air through water column. The model correctly simulated the Fe(II)-Fe(III) and As(III)-As(V) concentrations in the outlet waters and the precipitates, over hydraulic retention times from 50 min to 800 min. It confirmed that the natural attenuation at 20 °C was driven by the fast Fe(II) oxidation and slow As(III) oxidation that favored arsenite trapping by schwertmannite over amorphous ferric arsenate (AFA) formation. The localization of iron oxidation in the biofilm limited the attenuation of arsenic and iron as the water column height increased. The change in the composition of the bacterial iron-oxidizer community of the biofilm at the lowest pH boundary seems to control the Fe(II) oxidation kinetic rate besides the bacterial concentration.

Keywords. AMD, bioremediation, iron-oxidizing bacteria, HYTEC, reactive transport modeling.

Highlights.

- A reactive transport model for passive bioremediation of high-As acid mine drainage.
- The 2-D model captures the oxygen transfer through water to the reactive biofilm.
- Rate laws were obtained for microbial oxidation of Fe(II) and As(III) at different pH.
- Schwertmannite precipitation plays a key role on pH decrease and arsenite scavenging.
- Composition of the iron-oxidizing bacterial community controlled Fe(II) oxidation rate.

1. Introduction

Acid Mine Drainage (AMD) is one of the worst environmental hazards associated with post-mining. These acid leachates (pH 2 – 4) originate from the oxidation of sulfide minerals in mine tailings and waste piles. The phenomenon lasts hundreds of years after mine closure. It affects surface waters over long distances downstream from mining sites and it may compromise the safe use of freshwater resources. AMD contains iron and sulphate at concentration in the g L^{-1} range and toxic trace metals and

metalloids among which arsenic is of great concern due to its toxicity. Arsenic is ubiquitous in AMD, with concentrations ranging from tens of µg L^{-1} to hundreds of mg L^{-1} (Williams, 2001; Cheng et al., 2009). It is essential to develop remediation strategies able to assure long-term treatment of As-rich AMD with high performances and low maintenance cost. Passive treatment technologies based on natural attenuation processes are well suited to this scope (e.g. Johnson and Hallberg, 2005).

Microbial natural attenuation of arsenic has been described in many AMD worldwide (e.g. Cheng et al. 2009; Paikaray, 2015). It involves bacterial-mediated oxidation of aqueous ferrous species (Fe(II)) by oxygen into poorly soluble ferric (Fe(III)) phases. Bacterial oxidation of aqueous arsenite (As(III)) to arsenate (As(V)) also occurs in AMD and was shown to improve As retention efficiency (Maillot et al., 2013). The Fe-As solids include amorphous ferric arsenite and arsenate phases (Drahota et al., 2009; Maillot et al., 2013), As(III)- and As(V)-coprecipitated or adsorbed schwertmannite (Regenspurg et al., 2005; Paikaray et al., 2012; Maillot et al., 2013), crystallized scorodite (Langmuir et al, 2006) and tooeleite (Egal et al., 2009; Chai et al., 2016). The microbial oxidation rates of As and Fe in AMD streams are maximized by oxygen transfer (Savić et al., 1998; Sanchez-España et al., 2007; Chen and Jiang, 2012) and sheet-like flow in thin films (Gouin et al., 2013; Fernandez-Rojo et al., 2017).

All these processes can be exploited in passive engineered systems to treat As-rich AMD. Several field pilot-scale tests were conducted for the development of a first-step AMD treatment targeting arsenic and iron (Ahoranta et al., 2016; Fernandez-Rojo et al., 2019). The treatment conditions and system designs were usually not optimized, which led to variable and unpredictable efficiencies. The sizing and design of passive treatment systems requires the developments of numerical models able to represent the multiple coupled chemical and physical processes (e.g. Mayer et al., 2006; Indraratna et al., 2014).

Kinetic rate models were developed to describe microbial oxidation of ferrous iron in AMD, which is the key process at the base of natural arsenic attenuation. These microbial rate laws were obtained from lab results of batch and flow-through bioreactors (Pesic et al., 1989; Diz and Novak, 1999; Sheng et al., 2017; Yavari et al., 2019) or from in situ field ponds treating AMD from coal mines (Kirby et al., 1999). However, these studies did not explicitly consider neither the transport processes nor the sorption and coprecipitation of arsenic. Reactive transport models were developed to reproduce iron precipitation and partition of metal ions between solid and aqueous phases during neutralization of AMD by acid buffering minerals or during mixing with neutral pH waters (Berger et al., 2000; Tonkin et al., 2002; Balistrieri et al., 2003). However, in these studies, arsenic concentration was lower than 1 mg L^{-1}.

Gouin et al. (2013) developed a reactive transport model of Fe(II) removal and $Fe(OH)_3$ crust growth under thin film sheet flow applied to AMD in eastern Ohio (USA). Their two-dimensional model considered laminar sheet flow, the inclination of the sheet flow, oxygen transfer inside the water film all along the air-liquid interface, kinetics of Fe(II) oxidation and $Fe(OH)_3$ precipitation. They did not consider neither bacteria biofilm (bacteria were assumed to be uniformly distributed in the liquid phase only), more representative Fe(III) minerals such as schwermannite, nor arsenic chemistry. Their finding implied that simulation and prediction of such a complex biogeochemical AMD dynamic system required a reactive transport approach. To our knowledge, only Asta et al. (2010) developed a reactive transport model on arsenic and iron natural attenuation observed along an AMD discharge from the Iberian pyrite belt. The pH ranged from 2.9 to 3.5. The aqueous concentrations of Fe(II), As(III) and As(V) were about 600 mg L^{-1}, 1 mg L^{-1} and 1 mg L^{-1}, respectively. 1D-simulations were carried out with the PHREEQC code by coupling advective/dispersive transport, microbial oxidation of iron and arsenic, precipitation of schwertmannite and sorption of arsenate. Sorption was not modeled by surface complexation modeling but an empirical distribution coefficient (k_d) was used. The model successfully reproduced the major chemical trends and highlighted the good match between the rate constants of ferrous iron oxidation obtained with the reactive transport model and the values from the literature. On the contrary, the upscaling of rate constants of arsenite oxidation obtained at the laboratory was required to reproduce the field data.

In the present study, a reactive transport model is developed with the HYTEC code to simulate a consistent set of previous batch and flow-through experiments (Fernandez-Rojo et al., 2017; 2018; Tardy et al., 2018). These bioreactors reproduce the main natural processes of arsenic attenuation in high-As AMD at the Carnoulès mine in Southern France (Casiot et al., 2003; Morin et al., 2003; Egal et al., 2010). The nature of the solid phases that form upon ferrous iron and arsenite oxidation at the Carnoulès mine (Fernandez-Rojo et al., 2017; 2018) differs substantially from the study of Asta et al. (2010), partly due the higher arsenic content (about 40 mg L^{-1} instead of 2 mg L^{-1}). The 2D-model accounts for the fact that microbial oxidation takes place inside the bacterial biofilm only, rather than along the water column. This is an important issue for exploitation of natural attenuation in a passive biological treatment which does not use mechanical stirring or forced aeration for mass transfer. The aim of the model is to improve our understanding of how different biogeochemical and hydrodynamical factors affect the efficiency of the natural attenuation process. It will be used to improve the design and scaling of future AMD passive treatment pilot test performed at the Carnoulès site.

2. Experiments and modeling features

2.1. Batch and flow-through experiments

For the sake of clarity, the set of experiments that were modeled in the present paper are briefly presented in this section. The batch experiment of Tardy et al. (2018) is modeled as a base case for investigating the kinetics of the microbial oxidation of ferrous iron in AMD waters directly sampled from the Carnoulès mine. As shown in **Table 1** (the *B* model), the AMD water is slightly acidic with a pH of 4.7, and it has a high content in ferrous iron (511 mg L^{-1}), arsenite (46 mg L^{-1}) and sulfates (2 000 mg L^{-1}). The AMD water was incubated during 8 days at 20 °C in open flasks with continuous stirring. The pH and the concentration of dissolved O_2, Fe(II), total Fe, As(III) and As(V) were measured periodically. The Fe and As content, as well as the As(III)/As(V) distribution of the accumulated precipitates were also determined at the end of the experiment. The bacterial community was dominated by iron-oxidizing bacteria (92%) belonging to the genus *Gallionella*, whereas arsenic-oxidizing bacteria belonging to *Thiomonas* genus were present in minor proportion.

A series of flow-through experiments is modeled in a second step. They were carried out in bench-scale thermo-regulated rectangular channels (1 m length × 0.06 m width × 0.06 m depth) by Fernandez-Rojo et al. (2017, 2018). The experimental setup (**Fig. 1a**) mimicked the shallow sheet flow commonly seen across natural terraced iron formations (TIFs) occurring in AMD (Sanchez-España et al., 2007; Brown et al., 2011; Larson et al., 2014). It was composed of four channels connected in parallel through which the AMD water from Carnoulès was injected at constant flow rate. In a preliminary stage, the channels were fed at a given flow rate and at 4 mm water height up to reach steady state in terms of outlet Fe(II) composition and a bioprecipitate (biofilm, **Fig. 1b**) formed at the bottom of the channel containing As(III) and Fe(II) oxidizing bacteria that catalyzed the corresponding oxidation reaction. The initiation stage is not simulated in this paper.

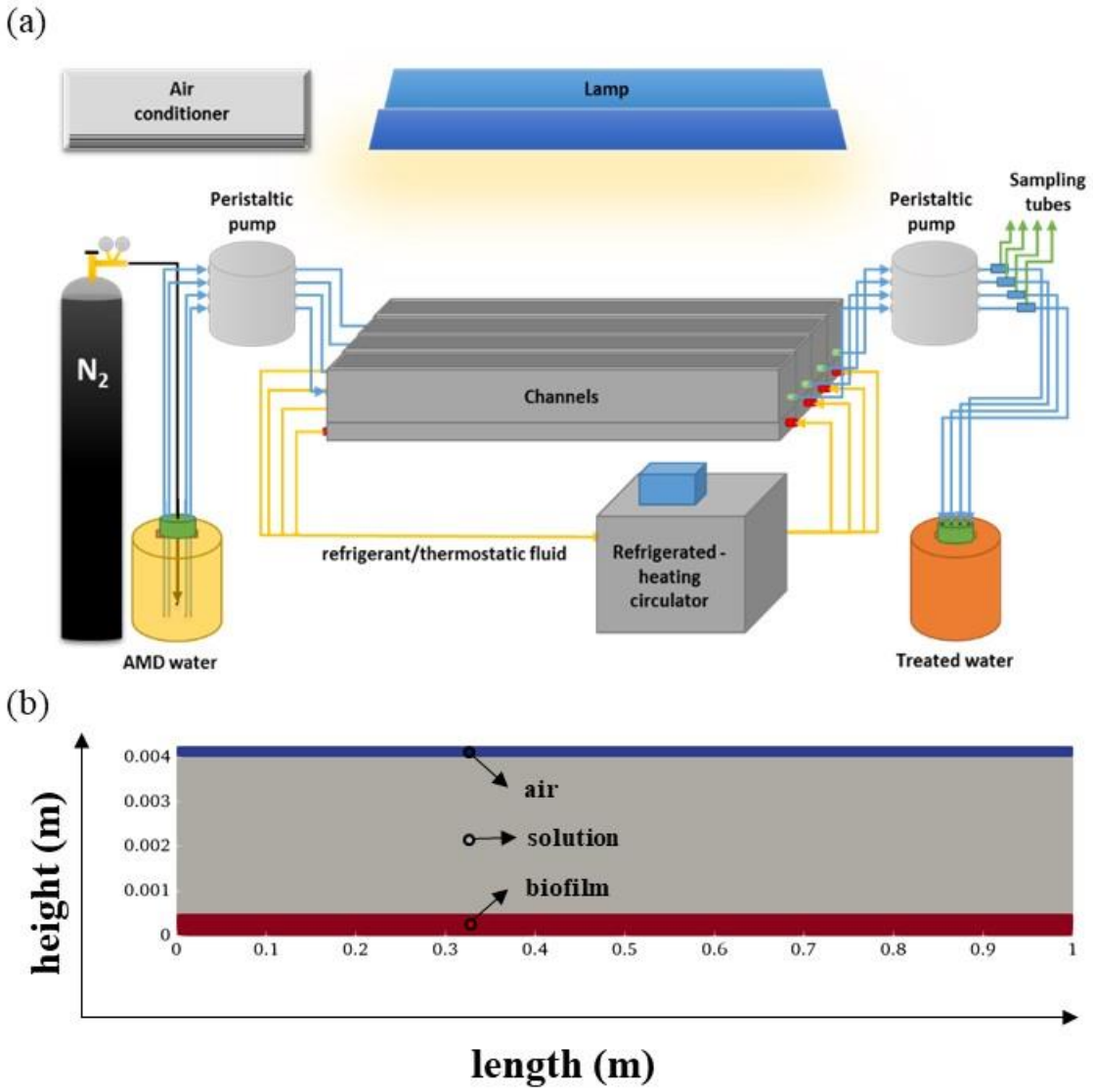

Figure 1. Experimental setup used in flow-through experiments according to Fernandez-Rojo et al. (2017) (a) and 2D longitudinal profile showing the channel zone distribution (b).

Four channels at 4 mm water height were then used in parallel to assess the effect of the hydraulic retention time (HRT) from 30 min to 600 min (the *FT4-3.9* model in **Table 1**). HRT was adjusted by changing the flow rate, however the latter always remained sufficiently low to maintain laminar flow conditions in the channel. Water chemistry was monitored during 19 days and, after this time, the precipitate accumulated in the first half and second half of the channels was recovered to further chemical and mineralogical analysis. The bacterial community in the biogenic precipitate was analyzed. It was dominated by Fe-oxidizing bacteria whatever the HRT. The proportion of *Gallionella* and *Ferrovum* genera shifted from respectively 65% and 12% at low HRT to 23% and 51% at high HRT, in relation with pH decrease from 3.2 to 2.8. Arsenic-oxidizing bacteria belonging to *Thiomonas* genus were present in minor proportion (2-3%) (Fernandez-Rojo et al., 2018). To evaluate the water height effect, two complementary experiments (models *FT4-3.4* and *FT25-3.4* in **Table 1**) were carried out in parallel with the same residence time but different water heights (4 mm and 25 mm). Dissolved oxygen concentration profiles were recorded through the water film height. In both cases, water and solid chemistry was analyzed once steady state was reached regarding Fe(II) composition in the outlet for a given residence time. Finally, the influence of the inlet pH on the arsenic removal was also evaluated by comparing models of experiments run under the same experimental conditions but decreasing inlet pH values from 3.9 to 3.1, as shown in **Table 1**. In experiments Exp 1 and Exp 2 used for model FT4-

3.1 and model FT4-3.4, the composition of the bacterial community was not analyzed but the genetic fingerprint showed distinct bacterial community structures between these two experiments, both in the inlet water and in the biogenic precipitates (Fernandez-Rojo et al., 2018).

Table 1. Experimental conditions, input chemistry and transport parameters used in the models.

Model label (1)		***B***	***FT***			
			FT4-3.9	***FT4-3.4***	***FT25-3.4***	***FT4-3.1***
EXPERIMENTAL CONDITIONS						
Experiment (2)		*T 20* (a)	*C1-C4* (b)	*Exp2 (4mm)* (c)	*Exp2 (25mm)* (c)	*Exp1 (OA)* (c)
Temperature *T*	°C	20				
Flow rate *Q*	mL min^{-1}	-	0.4 – 8	0.3 – 8	1.9 – 50	0.4 – 8
Hydraulic retention time *HRT*	min	-	600 – 30	800 – 30	802 – 30	600 – 30
Channel height	mm	-	4	4	25	4
Duration	days	8	19	19	19	19
INPUT CHEMISTRY						
pH		4.7	3.9	3.4	3.4	3.1
Fe(II)	mg L^{-1}	511	460	480	476	432
Fe(III)	mg L^{-1}	1	1	4	6	9
As(III)	mg L^{-1}	46	34	30	33	19
As(V)	mg L^{-1}	7	6	6	6	12
SO_4^{2-}	mg L^{-1}	2000	1795	1900	1900	1801
$O_{2(aq)}$	mg L^{-1}	7.8	4.8	4.8	3.5	3.2
TRANSPORT PARAMETERS						
Porosity ω		-	1	1	1	1
Fluid velocity *U*	m s^{-1}	-	2.8×10^{-5} – 5.6×10^{-4}	2.1×10^{-5} – 5.6×10^{-4}	2.1×10^{-5} – 5.6×10^{-4}	2.8×10^{-5} – 5.6×10^{-4}
Dispersivity α (3)	m	-	5×10^{-5}	5×10^{-5}	7×10^{-4}	5×10^{-5}
Diffusion Coefficient D_e	m^2 s^{-1}	-	2×10^{-9}	2×10^{-9}	2×10^{-9}	2×10^{-9}

(1) Labels of the models are coded by type of experiment (*B* = batch experiment, *FT* = flow-through experiment). The labels of the *FT* models are sub-coded by water height (4 mm or 25 mm) and input pH (3.1, 3.4 and 3.9). (2) Experiments of (a) Tardy et al. (2018), (b) Fernandez-Rojo et al. (2018), (c) Fernandez-Rojo et al. (2017). (3) The dispersivity is a scalar in the present modeling, i.e. identical for both longitudinal and transverse dispersivities.

2.2. The reactive transport equation

The HYTEC formulation of the multicomponent reactive transport relevant for the channel configuration is (van der Lee et al., 2003):

$$\frac{\partial \omega [E_i]}{\partial t} = div\,(D_d\, \boldsymbol{grad}\,[E_i] - [E_i]\,\boldsymbol{U}) - \frac{\partial \omega\, \overline{[E_I]}}{\partial t} \qquad (1)$$

where $[E_i]$ is the total mobile (i.e. dissolved in the aqueous solution) concentration of an element *i* per unit volume of solution, and $[\overline{E_I}]$ is the immobile (i.e. sorbed or in minerals) concentration of an element *i* per unit volume of solution, ω is the porosity, and *U* is the Darcy velocity. The partial derivative term $-\frac{\partial \omega\, \overline{[E_I]}}{\partial t}$ is driven by the chemical reactions whereas the other terms are linked to the transport processes (advection/dispersion and/or diffusion). The term D_d is the effective diffusion/dispersion coefficient

$$D_d = D_e + \alpha \|\boldsymbol{U}\| \quad (2)$$

with α the scalar hydrodynamic dispersivity and D_e the scalar effective diffusion coefficient. From a numerical point of view, chemistry and transport are coupled through a sequential iterative algorithm. The transport module is based on the representative elementary volume (REV) approach with finite volume calculation. HYTEC takes into account all the chemical reactions in aqueous solution. In the present case, the relevant reactions are mainly redox reactions, acid/base reactions and ion complexation in solution, as well as precipitation of solid phases. HYTEC can also model the kinetics of different types of reactions, such as redox reactions in solution or dissolution/precipitation of minerals. Kinetics of As and Fe redox oxidation were taken into account in the present study.

Thus, the different HYTEC features have the ability to consider both chemical reactions and transport processes. They also enable involving the microbial activity in the transformation process. This was introduced in the model by considering the action of microorganisms on reaction rates (see section 2.4) and the localization of microorganisms in the biofilm zone in the 2D simulation grid (see section 2.5). This was the first application of the HYTEC code to the modeling of chemical, microbial and transport processes involved in natural attenuation of Fe and As in AMD.

2.3. Thermodynamic data

The thermodynamic database Thermoddem (Blanc et al., 2012) was used in all simulations. This database gathers the formation constants of aqueous species, gases and a wide set of mineral phases from wastes and natural environments. According to Fernandez-Rojo et al. (2017, 2018), the most relevant mineralogical processes considered in the modeling were i) the formation of an amorphous Fe(III)-arsenate (AFA), with a stoichiometry similar to scorodite ($FeAsO_4{:}2H_2O$), and ii) the co-precipitation of As(III) with schwertmannite ($Fe_8O_8(OH)_6(SO_4){:}8H_2O$).

The solubility of an amorphous phase cannot generally be determined with accuracy. In this study, the formation constant of the amorphous Fe(III)-arsenate AFA was slightly increased from the Thermoddem constant $10^{4.5}$ to $10^{5.3}$ (**Table 2**) to better fit the batch and flow-through experimental data, as shown in **Fig. 2**. The higher the formation constant, the lower the solubility product. This increase of the mineral stability is supported by different studies from the literature that considered formation constants of AFA up to $10^{6.5}$ (Langmuir et al., 2006; Paktunc et al., 2010).

It is well known that poorly ordered nano-crystalline hydroxy-sulfate minerals of microbial origin, such as schwertmannite, are important arsenic scavengers in sulfate-rich acid mine drainage environments. But the actual arsenic retention mechanism, sorption (Burton et al., 2009; Maillot et al., 2013, Paikaray et al., 2014) or co-precipitation (Egal et al., 2009; Park et al., 2016), depends on the AMD environments. Furthermore, Burton et al. (2009) and Liao et al. (2011) showed that As(III) sorption at high As concentration proceeds to a large extent via an exchange mechanism into the schwertmannite tunnel structure between $H_2AsO_3^-$ and SO_4^{2-} (and to a lesser extent OH^-), rather than merely surface complexation at the mineral-water interface. The empirical sorption isotherms (K_d, Langmuir) are only applicable at a given pH value (Burton et al., 2009; Liao et al., 2011; Paikaray et al., 2012). To our knowledge, there is no thermodynamic constants in the literature for sorption mechanisms of As(III) on schwertmannite that can be implemented in reactive transport model. In addition, the specific surface of the schwertmannite crystals for As(III) sorption can vary to a large extent (Paikaray et al., 2012) and is tricky to be measured in biofilms. Since the main goal of this paper is to investigate the coupling between the reactions (oxidation, precipitation) and the transport (advective flow, O_2 supply), and for the sake of simplicity, the stoichiometry of the As(III)-schwertmannite mineral (**Table 2**) was set in order to globally respect the As/Fe molar ratio (1/8) measured in the solid phases at the end of the batch experiment (**Section 3.1**). This stoichiometry is only suitable for the present AMD waters with a high As content (about 50 mg L^{-1}). The As(III)/Fe mole ratio of 0.125 is within the range

of ratios 0.080 – 0.150 found by Burton et al. (2009) at high As concentrations and pH 4. The formation constant of the As(III)-schwertmannite was then adjusted to fit the data of the present batch and flow-through experiments, as shown in **Fig. 2**.

The two stability or phase diagrams of **Fig. 2** give the boundary between the dominant Fe(III) aqueous species and the solid phase (e.g. schwertmannite). The complex $FeSO_4^+$ stands for more than 90% of the total Fe(III) aqueous concentration under the present chemical conditions. The diagrams also provide for the comparison of the stability of different Fe(III)-minerals with respect to the pH and the activity of the main Fe(III) species. For the sake of comparison, **Fig. 2** gives the stability domain of pure schwertmannite without any As incorporation. In the literature, the solubility product of schwertmannite is either around log K_s = 9 – 10 or around log K_s = 18 – 19. The Thermoddem database has a log K_s = 9.0, close to the log K_s = 10.5 ± 2.5 of Yu et al. (1999) obtained for natural stream waters polluted by mine drainage. Bigham et al., (1996) found a log K_s = 18.0 ± 2.5 for mine drainage solutions with pH values in the range 2.8 – 4.5. Regenspurg and Peiffer (2005) measured a log K_s = 18.5 for synthetized schwertmannite in solution at pH 2 and 4. Sánchez-España et al. (2011) reported a log K_s = 18.8 ± 1.7 obtained by pH titration at the laboratory in the pH range 3.0 – 3.5. The latter constant was selected by Larson et al. (2014) to investigate thermodynamic control on the kinetics of microbial low-pH Fe(II) oxidation. The present data also agree relatively well with the constant of Sánchez-España et al. (2011), maybe because it would correspond to a highly hydrated schwertmannite as proposed by those authors.

Table 2. Formation constants K_f (the inverse of the solubility product K_s) of the precipitated solids considered in the modeling of the batch and flow-through experiments.

Proxy for As(III)-schwertmannite (1) – responsible of As(III) scavenging	
Reaction of formation	$8Fe^{3+} + H_2AsO_3^- + 21H_2O + SO_4^{2-} \rightarrow Fe_8O_8(OH)_5(H_2AsO_3)(SO_4) \cdot 8H_2O\ (s) + 21H^+$
log K_f (20°C)	-8.9
Amorphous ferric arsenate (AFA) – responsible of As(V) scavenging	
Reaction of formation	$Fe^{3+} + H_2AsO_4^- + 2H_2O \rightarrow FeAsO_4 \cdot 2H_2O\ (s) + 2H^+$
log K_f (20°C)	5.3

(1) The phase diagram of Fig. 2 also considers the formation of pure schwertmannite for comparison: $8Fe^{3+} + 22H_2O + SO_4^{2-} \rightarrow Fe_8O_8(OH)_6(SO_4) \cdot 8H_2O\ (s) + 22H^+$; log K_f (25°C) = -9.0 or -18.8 (see Sec. 2.3).

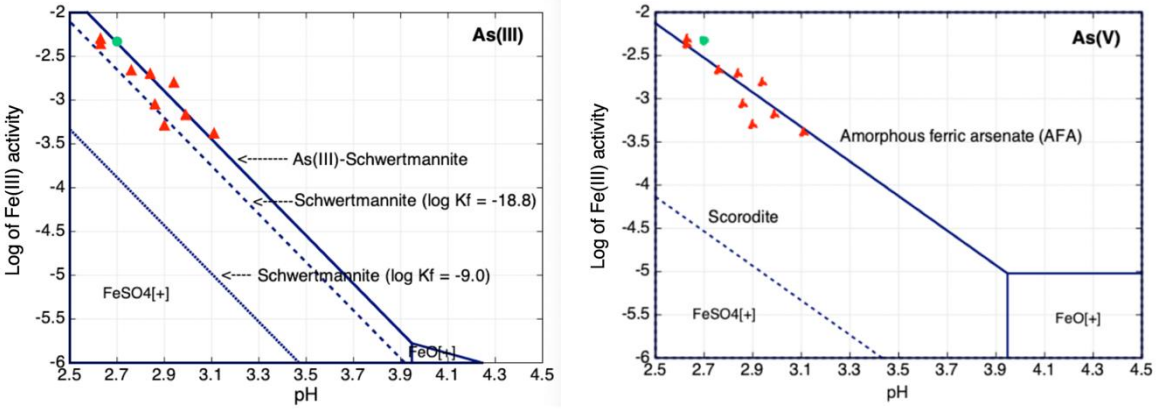

Figure 2. Simplified stability diagrams of the As(III) and As(V) precipitates considered with respect to Fe(III) activity in the modeling with some data on the total Fe(III) concentration of the batch (in green)

and flow-through (in red) experiments (temperature = 20°C, activity of SO_4^{2-} = 10^{-2}, total H_3AsO_3 = 10^{-3} M, total H_4AsO_4 = 10^{-6} M).

2.4. Kinetics of microbial oxidation

Whatever the transport control process (static batch versus dynamic flow-through), the most important reaction is the oxidation of ferrous iron by the dissolved oxygen in solution:

$$Fe^{2+} + 0.25\, O_2(aq) + H^+ \rightarrow 0.5\, H_2O + Fe^{3+} \quad (4)$$

where one mole of electron is transferred per mole of Fe^{2+} to the electron acceptor which is the dioxygen dissolved in the solution. The abiotic oxidation of Fe(II) can be neglected since its rate is several orders lower than the rate of the microbially mediated oxidation in the studied pH range 2.5 – 4.5 (Larson et al., 2014). The following second-order kinetic rate law was assigned to the microbial oxidation reaction:

$$r_{Fe} = \frac{d[Fe(II)]}{dt} = -\, k_{Fe}[Fe^{2+}][O_2(aq)] \quad (5)$$

where k_{Fe} is the kinetic rate constant and the brackets stands for the concentrations of the species. The rate constant was fitted onto the total concentration of Fe(II) species given by the chemical analysis, i.e. essentially the sum of the aqueous concentration of Fe^{2+} and $FeSO_4$ according to the modeling under the chemical compositions of the present AMD waters. The right member of **Eq. (5)** takes only into account Fe^{2+} as the active species for the microbial reaction in the reactive transport code HYTEC. The modeling showed that $[Fe^{2+}]$ counted for about one half of the total concentration. Therefore, the rate constant k_{Fe} would be twice lower if $[Fe(II)]$ was taken instead of $[Fe^{2+}]$ in the second order reaction.

Asta et al. (2010) considered a kinetic rate law similar to **Eq. (5)**, but the partial pressure of the oxygen gas, $p_{O_2(g)}$, was used instead of the aqueous concentration of O_2. The latter was preferred in the present 2D-modeling which explicitly simulated the dissolution and transfer of oxygen from the air towards the biofilm through the water film. The linear relationship of the oxidation rate with respect to the concentration of Fe(II) and dissolved oxygen has been validated by Pesic et al., 1989 for Fe(II) concentration in the range of 0.100 g/L, pH > 2.2, T = 25°C, and oxygen concentration close to the equilibrium with the atmospheric partial pressure. Kinetic rate independent of Fe(II) may become applicable for Fe(II) concentration above 1 g/L (Karamanev and Nikolov, 1988; Noike et al., 1988). Therefore, a Monod kinetic expression on the Fe(II) concentration would be required to simulate AMD effluents with both moderate and high Fe(II) concentrations. With respect to the effect of oxygen, Sânchez-Espana et al. (2007) measured that the Fe(II) oxidation rate was faster under atmospheric oxygen-saturated conditions.

Beside Fe(II) concentration and oxygen, several authors (Pesic et al., 1989; Kirby et al., 1999; Sheng et al., 2017) implemented a four-order reaction with the additional dependency of the kinetic rate upon the concentration of proton, $[H^+]$, and the concentration of Fe(II)-oxidizing bacteria, [bacteria]. This clearly works for a single type of bacteria, such as in Pesic et al. (1989). But in the present study, it was not obvious to quantify the proportion of active bacteria within the microbial population of the biofilm from the one hand, and the types of bacteria in the biofilm evolved with the pH from the other hand. As Larson et al. (2014), $[H^+]$ had been explicitly removed from the rate equation such that the effect of pH can be evaluated separately. As shown in **Table 3**, the kinetic rate constant k_{Fe} was first fitted on the first set of flow-through experiments (*FT4-3.9)* with an initial pH_i of 3.9. This rate constant was then extrapolated to the three other sets of flow-through experiments (*FT4-3.4*, *FT25-3.4* and *FT4-3.1*) on the basis of a linear dependency with the initial concentration of proton $[H^+]$ in the input solution:

$$k_{pH_i} = k_{pH_i=3.9} \frac{[H^+]_i}{10^{-3.9}} \quad (6)$$

The effects of the bacteria concentration and pH on the kinetics of Fe(II) oxidation are discussed in details in **Section 4**.

A similar approach was pursued for the microbial oxidation of arsenite by the dissolved dioxygen,

$$H_3AsO_3 + 0.5\ O_2(aq) \rightarrow H_2AsO_4^- + H^+ \quad (7)$$

where 2 moles of electron is transferred per mole of H_3AsO_3 to the same electron acceptor, i.e. the dioxygen dissolved in the solution. A second-order kinetic law was also selected for this reaction:

$$r_{As} = \frac{d[As(III)]}{dt} = -k_{As}[H_3AsO_3][O_2(aq)] \quad (8)$$

The modeling showed that H_3AsO_3 was the principal As(III) species in solution with respect to the pH range (2.5 – 4.5) of this study.

The kinetically-controlled reactions of Fe^{2+} and H_3AsO_3 exclusively occurred in the biofilm in the reactive transport model. They were decoupled (i.e. fitted independently) since they were driven by different types of bacteria in the biofilm (Fernandez-Rojo et al., 2018). The kinetic rate constants k_{Fe} and k_{As} were the fitting parameters of the model (**Table 3**). For the sake of minimizing the number of modeling parameters, the precipitation reactions of **Section 2.3** were simulated under thermodynamic equilibrium only.

It is worth mentioning that the possible oxidation of As(III) by Fe(III) (Asta et al. 2010; 2012) was not considered in the modeling for three reasons. There was less than 1% dissolved Fe under Fe(III) form in the waters of Carnoulès AMD. There was no UV irradiation under the present lab conditions, whereas the oxidation of As(III) by Fe(III) depends on reaction intermediates that are activated by UV only. Eventually, the microbial oxidation of As (III) in the waters of Carnoulès AMD did not occur when the water was inoculated with *A. ferrooxidans* bacteria that only oxidized Fe(II) to Fe (III) (Egal et al., 2009).

Table 3. Kinetic rate constants considered in the modeling of the batch (*B*) and flow-through (*FT*) experiments.

Model	***B***	***FT***			
		FT4-3.9	***FT4-3.4***	***FT25-3.4***	***FT4-3.1***
Input pH	4.7	3.9	3.4	3.4	3.1
Output pH [(a)]	2.8	3.0 ± 0.2	3.0 ± 0.1	3.0 ± 0.1	3.1 ± 0.1
Fe(II) oxidation kinetics, Eq. (5)					
k_{Fe} (L mol^{-1} s^{-1})	2.7×10^{-2} [(b)]	5 [(b)]	15.8 [(c)]	15.8 [(c)]	31.6 [(c)]
As(III) oxidation kinetics, Eq. (8)					
k_{As} (L mol^{-1} s^{-1})	≤ 5×10^{-6} [(b)]	≤ 0.5 [(b)]	≤ 0.5 [(b)]	≤ 0.5 [(b)]	≤ 0.5 [(b)]

(a) The output pH of the *B* model corresponds to the pH at the end of the batch experiment (after 6 days). The output pH of *FT* models indicates the average of the output pH values obtained at the different hydraulic retention times (HRT). (b) Fitted constant. (c) Extrapolated constant according to Eq. (6).

2.5. Simulation grid and transport parameters

The batch experiment was modeled with the geochemical module of HYTEC, assuming that the volume of solution was instantaneous homogenized within a single grid node. The flow-through experiments were modeled with a 2D simulation grid composed of three zones (shown in **Fig. 1b**) with regular discretized nodes of 5×10^{-2} m (X direction, length) by 2.5×10^{-4} m (Y direction, height). At the bottom of the channel, the biofilm was represented by a thin layer of 0.5 mm height and 1 m length. The kinetics of arsenic and iron oxidation by the bacteria could only occur in this zone. The main zone representing the solution had a different height depending on the model (4 mm or 25 mm). The upper zone (0.25 mm thick) representing the air-solution interface accounted for thermodynamic equilibrium of the solution in this zone with atmospheric air (Henry's law). The kinetics of atmospheric oxygen dissolution into the solution was not considered in the models.

The fluid velocities U (m s^{-1}) was fixed as input boundary conditions (**Table 1**). They were obtained by dividing the flow rate Q (m^3 s^{-1}) used in the experiments by the cross section S (m) of the solution in the channel. The hydraulic retention time HRT (s) was calculated dividing the volume V (m^3) of the solution by the flow rate Q (m^3 s^{-1}) used in the experiments. The diffusion coefficient was set to 2×10^{-9} m^2 s^{-1} for all dissolved species in the model. As discussed in **Section 4.2**, diffusion of dissolved oxygen in the water film was not sufficient by itself to account for the whole oxygen transfer from the air/solution interface down to the biofilm. Dispersion was also required. The scalar dispersivities set for the 4 mm and 25 mm water heights were 5×10^{-5} m (in the range of the numerical dispersivity of the grid) and 7×10^{-4} m, respectively (see **Section 4.2**).

2.6. Input and boundary chemical conditions

The chemistry of the inlet water defined in the models as well as that one injected in the experiments corresponded to the AMD water collected from the source of the Reigous Creek at the Carnoulès mine. Their aqueous chemistry depends on the sampling campaign (**Table 1**), with Fe(II) concentrations ranging from 432 to 511 mg L^{-1} and As(III) concentration ranging from 19 to 46 mg L^{-1}. The waters also contain As(V) but at a lower level of concentration, from 6 to 12 mg L^{-1}. The sulfate concentration is always high, ranging from 1 795 to 2 000 mg L^{-1}. It is worth noting that some of these *a priori* not significant differences in composition could influence the efficiency of the As bioremediation process, as discussed in **Section 4.3**.

The concentration of dissolved oxygen $[O_2(aq)]$ in the input solution was measured to be equal to 7.8 ± 0.5 mg O_2 L^{-1} in the batch experiment (close to atmospheric equilibrium) and around 4 mg O_2 L^{-1} in the flow-through experiments (**Table 1**). In the latter experiments, the input solution was not in equilibrium with respect to the atmospheric air given that fluid containers at the inlet were partly purged with N_2 in order to avoid iron pre-oxidation.

During the batch experiment, the agitation applied during the experiment promoted a constant $[O_2(aq)]$ in equilibrium with the atmospheric air during the entire elapsed time. Accordingly, a constant partial pressure of oxygen was fixed at 0.2 atm in the modeling of the batch experiment. In the flow-through experiments, $[O_2(aq)]$ was measured at the outlet over time. In complement, $[O_2(aq)]$ profiles perpendicular to the flow direction were also recorded along water columns located at the inlet/outlet of the channel. In the reactive transport model, the dissolved oxygen profiles throughout the channels were the combination of two mass transfer processes: (1) the horizontal advective/dispersive flow imposed at the inlet of the channel as an input boundary condition and (2) the vertical mainly diffusive transfer from the air-solution interface to the bottom of the channel. This upper interface of the simulation grid was characterized by a condition of constant partial pressure of oxygen of 0.2 atm.

3. Modeling results

The modeling results related to bioremediation of As-rich acid main drainage in the batch (*B* model) and flow-through reactors (*FT* models) are presented in this section. The four *FT* models reproduce the same type of flow-through experiment but in each model one specific parameter is changed (such as the water height or the input pH) to evaluate its influence on the overall removal of As and Fe. Hence, a complete and detailed presentation of the modeling results obtained is presented for one of the four *FT* models (*FT4-3.9* model) in order to avoid repetitive information. Modeling results obtained from the other three *FT* models are presented in **Section 4** to discuss the parameters controlling the natural attenuation of arsenic and iron in acid mine drainage.

All models performed except one successfully reproduce the results obtained at laboratory scale by using the same thermodynamic of secondary phases and the same kinetic rate laws for the Fe and As oxidation reactions. The *FT4-3.1* model is the unique model that presents some discrepancies between the modeling and the experimental data which are properly discussed in **Section 4**.

3.1. Modeling of the batch experiment (*B* model)

The modeling results of the batch experiment are presented in **Fig. 3** (brown-solid lines) and **Table 4**. The *B* model includes the redox reactions of **Eqs. (4)** and **(7)** as well as the precipitation reactions of **Table 2**. This model mimics the experimental data satisfactorily, reproducing both aqueous and solid chemistry patterns. The batch experiments lasted 8 days but the *B* model considers 6 days of AMD water incubation. In the first two days of experiment water chemistry did not vary at all since the bacteria responsible of catalyzing the oxidation reactions needs some time for adaptation to the new environment.

The kinetic rate constants k_{Fe} and k_{As} used in the *B* model to fit the modeling and the experimental data are 2.7×10^{-2} L mol^{-1} s^{-1} and 5×10^{-6} L mol^{-1} s^{-1}, respectively (**Table 3**). Slight changes in k_{Fe} provoked significant variations in water chemistry, whereas the k_{As} value could be modified by orders of magnitude without affecting the chemical composition. For $k_{As} \leq 5\times10^{-6}$ L mol^{-1} s^{-1} the modeling results match well with the experimental data in which no arsenic oxidation occurred.

The pH was not monitored during the experiment but inlet and outlet pH were measured showing a decrease in pH from 4.7 to 2.8. In the model, pH decreases sharply during the first hours to remain practically constant (pH about 2.9) until the end of the experiment. The final simulated pH coincides with the measured value (Fig. 3a). The temporal evolution of the aqueous iron and arsenic concentrations obtained from the model matches well with the measured data (Fig. 3b, c). The aqueous Fe(II) concentration decreases with time due to iron oxidation. Sânchez-Espana et al. (2007) obtained a similar evolution of Fe(II) concentration in laboratory batch experiments performed with aliquots AMD mine effluents. The aqueous Fe(III) concentration increases with time as a result of the iron oxidation reaction, but it is also controlled by the subsequent precipitation of As(III)-schwertmannite. Regarding the evolution of the arsenic species, the concentration of aqueous As(III) significantly decreases with time whereas the concentration of As(V) only slightly decreases.

The *B* model was modified by do not considering precipitation reactions in order to (1) verify that, as presented in Tardy et al. (2018), there is no arsenic oxidation under these experimental conditions and, (2) check the effect of precipitation on the pH evolution. Indeed, the modified *B* model (orange-dotted lines in **Fig. 3**) shows a constant concentration of aqueous As(III) and As(V) during the elapsed time that indicates no arsenic oxidation (**Fig. 3c**). There is only a slight decrease in pH, from 4.7 to 3.9 (**Fig. 3a**) suggesting that the significant decrease in pH observed in the experiments (from 4.7 to 2.8) was due to the precipitation of As(III)-schwertmannite that releases a large number of H^+ (**Table 2**).

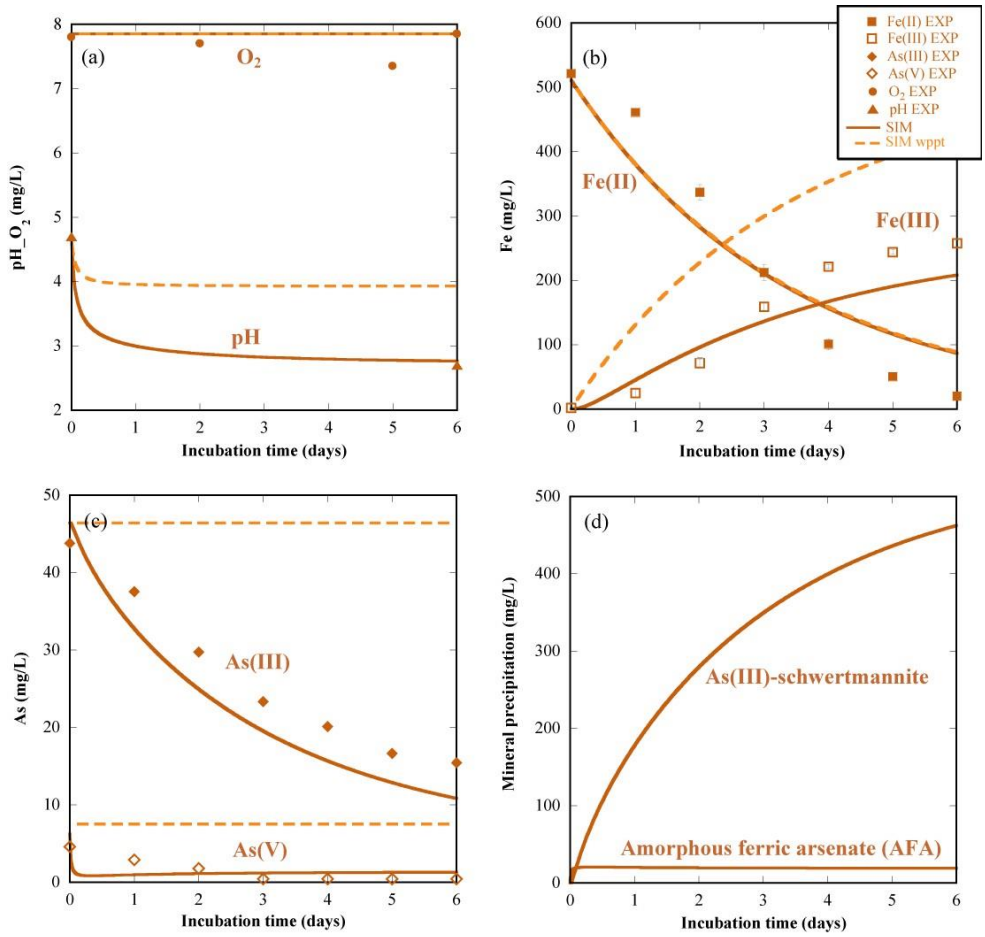

Figure 3. Variation in pH, concentration of O_2, Fe(II), Fe(III), As(III) and As(V) and amount of precipitated As(III)-schwertmannite and amorphous ferric arsenate (AFA) versus time obtained from the *B* model (SIM; lines) and compared with the measured data (EXP; points) from the *T20* batch experiment run in Tardy et al. (2018). Brown-solid and orange-dotted lines indicate modeling results with mineral precipitation (SIM) and without mineral precipitation (SIM_wppt), respectively.

The concentration of mineral precipitated obtained from the model (**Fig. 3d**) provided particulate Fe and As (As(III), As(V)) concentration values after 6 days of incubation (**Table 4**). These values are in good agreement with the experimental data, in terms of concentrations but also in terms of As(III)/As(V) ratio and As/Fe ratio. As(III)-schwertmannite precipitates during all the experiment reducing the aqueous As(III) concentration from 46 to 11 mg L^{-1}, whereas AFA precipitates only at the very beginning of the experiment (low solubility) almost entirely eliminating the amount of aqueous As(V) in the AMD water. No additional AFA precipitation occurs given that arsenic oxidation is negligible in this experiment.

Table 4. Chemical concentration of the particulate matter (in mg L^{-1}) at the end of the experiment obtained from the *B* model (*SIM*) and compared with the measured data (*EXP*) from batch experiment *T20* run in Tardy et al. (2018).

	Concentration (mg L^{-1})				Mole ratio	
	total Fe	**total As**	**As(III)**	**As(V)**	**As/Fe**	**As(III)/As(V)**
EXP	232 ± 14	38.6 ± 1.6	33.4 ± 1.5	5.2 ± 0.1	0.125	6.5
SIM	217	41.9	35.6	6.2	0.144	5.7

3.2. Modeling of the flow-through experiments (*FT4-3.9* model)

The *FT4-3.9* model was performed to reproduce a set of 4 flow-through experiments run in parallel and at different flow rates by Fernandez-Rojo et al. (2018). The chemical composition measured in the outlet solution and in the particulate matter after 19 days of AMD water injection at constant flow rate is well reproduced by the model (**Fig. 4** and **Table 5**).

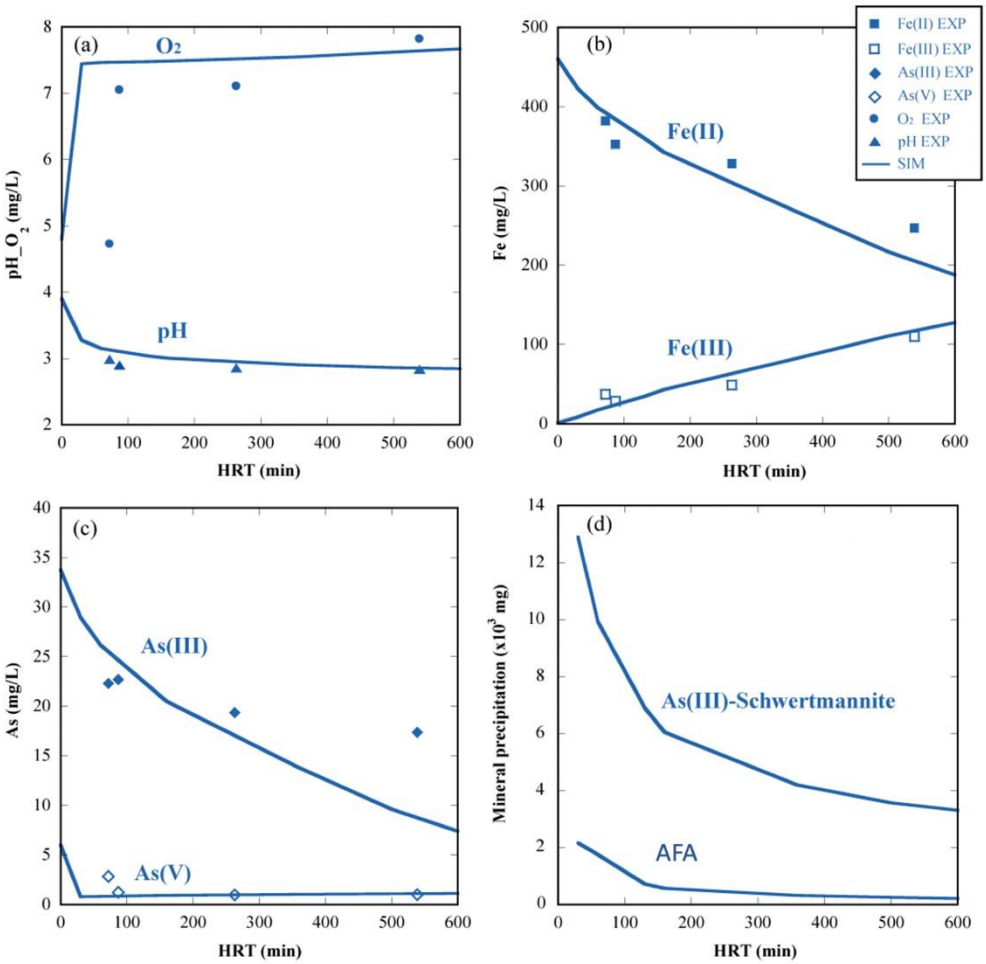

Figure 4. Variation in pH, concentration of O_2, Fe(II), Fe(III), As(III) and As(V) and amount of precipitated As(III)-schwertmannite and amorphous ferric arsenate (AFA) versus the hydraulic retention time (HRT) obtained from the *FT4-3.9* model (SIM; lines) and compared with the measured data (EXP; points) from experiments *c1* – *c4* of Fernandez-Rojo et al. (2018).

The kinetic rate constants k_{Fe} and k_{As} used in the *FT4-3.9* model to fit the experimental data are 5 L mol^{-1} s^{-1} and 0.5 L mol^{-1} s^{-1}, respectively (**Table 3**). The k_{Fe} value used in this model is two orders of magnitude higher than the value used to fit the batch experiment (*B* model). This fact is mainly related to the much larger amount of the catalyzing bacteria and, to a lesser extent, to the catalyzing efficiency in the biofilm (see **Section 4.3**). The k_{As} value corresponds to a 10 % of As(III) oxidation. The amount of As(III) oxidation was fixed in the model based on the experimental results obtained in the flow-through experiments (Fernandez-Rojo et al., 2018). The authors showed the evidence, not quantified, of little As(III) oxidation and a maximum of 10 % is assumed in models *FT*. For $k_{As} \leq 0.5$ L mol^{-1} s^{-1} the modeling results correctly simulate the experimental data and the percentage of arsenic oxidation is within the range 0 – 10 %.

The modeling correctly simulates the pH decreases from 3.9 to 3.0 ± 0.2 (**Fig. 4a**) while increasing the HRT and the subsequent increase of the performance of the bioreactor in terms of Fe(II) oxidation

and As abatement (**Fig. 4b, c**). Model also predicts well the decrease of precipitated mass with HRT increase, in particular for As(III)-schwertmannite (**Fig. 4d**).

Regarding the chemical composition of the biogenic precipitates deposited in the first half and second half of the channel, a comparison between modeling and experimental data is presented in **Table 5** for the experiment with HRT around 100 min. Two models are displayed in the table: the *SIM* model where precipitation, under thermodynamic equilibrium, can take place everywhere (both in the solution and the biofilm zones), and the *SIM-b* model where precipitation is forced to occur in the biofilm zone (where microbial oxidation reactions occur). Both simulations show very similar results suggesting that no spatial constraint of precipitation in the biofilm is needed in the model to reproduce the experimental results. Given the complexity of the system, the agreement of the model with the experimental data of the total mass of precipitates is fairly good. The experimental total masses of Fe and As that have precipitated stands for 64 wt.% and 59 wt.% of the calculated ones, respectively. Assuming that the oxidation of Fe(II) is the rate-limiting step for Fe removal process in both the model and the experiment, the present experimental precipitation rates of Fe and As are roughly 1.5 times to twice as low as the Fe(II) oxidation rate. Mineral precipitation occurred at thermodynamic equilibrium in the model whereas a slight kinetic constraint on precipitation took place in reality and limited the amount of precipitates. This issue of kinetics is discussed in **Section 4.2**. As(III)-schwertmannite precipitation is more localized at the first half of the channel in the experiment than in the model. The first half stands for 84 wt.% of the total Fe in the experiment for 58 wt.% in the model. However, the model also predict a significant precipitation of As(III)-schwertmannite at the beginning of the channel as shown in **Fig. 5** (and more clearly in the longitudinal profile of **Fig. SI-1**). The pH progressively decreases in from 3.5 to along the channel 3.0 in the biofilm in steady-state (**Fig. SI-1**), and the higher the pH, the lower the solubility of schwertmannite (**Fig. 2**).

Table 5. Experimental (*EXP*) and simulated (*SIM* and *SIM-b*, *FT4-3.9* model) chemical composition of the biogenic precipitate recovered from the channel bottom at the end of the flow-through experiment with hydraulic retention time (HRT) around 100 min.

	weight	total Fe	total As	As(III)	As(V)
	g	mg	mg	mg	mg
1st half of the channel					
EXP(1)	5.0	1818	398	302	95
SIM	4.5	1923	505	297	208
SIM-b	4.9	2042	602	305	296
2nd half of the channel					
EXP(1)	0.9	332	56	45	11
SIM	3.1	1417	261	234	27
SIM-b	3.2	1460	274	241	33
All the channel					
EXP(1)	5.9	2151	454	347	107
SIM	7.6	3340	766	531	235
SIM-b	8.1	3501	876	546	330

(1) The experimental values (in mg) were derived from concentrations (in mg g^{-1}) of Fe and As species in the biogenic precipitate (published in Fernandez-Rojo et al. (2018)) and total precipitate weight (unpublished data).

The modeling results provide also information about the spatial distribution of solution and solid chemistry throughout the bioreactor channel (**Fig. 5**). The profile of the solution chemistry reaches a steady state after 5 hours of injection. At this stage, the 2D longitudinal profile of the dissolved O_2 concentration shows a vertical decrease in concentration from the top to the bottom of the channel (**Fig. 5a; Fig. 7a**). In the model, the dissolved O_2 profile is the consequence of (1) the horizontal flow forced at the inlet of the channel, (2) the vertical O_2 diffusion from the air zone to the bottom of the channel,

and (3) the O_2 consumption by the bacteria present in the biofilm. Those modeling results are compared to the experimental data in **Section 4.2**. Likewise, the steady-state aqueous Fe(II) concentration that decreases along the channel results from the inlet flow and the Fe(II) consumption by the bacteria (**Fig. 5b**). There is no experimental data on the spatial distribution of dissolved Fe(II) in the water film in the present experiments. However, unpublished data from another set of experiments **(Fig. SI-2)** show a progressive decrease of dissolved Fe(II) concentration along the channel length). The 2D longitudinal profile of As(III)-schwertmannite precipitates regularly accumulates in the biofilm zone until the end of the experiment. As observed in **Fig. 5c**, As(III)-schwertmannite precipitation is distributed all along the channel in the biofilm zone but is slightly more localized in the first half of the channel. The comparison with experimental data on the location of precipitates has been made in the previous paragraph. It is worth noting that despite high concentrations in As(III)-schwertmannite such as 350 g/L in **Fig. 5c**, the corresponding total mass of precipitates in the channel remains in the order of a dozen of grams (see **Table 5**) since the total volume of the biofilm in Liter is quite small. The maximal concentration of 350 g/L corresponds to 0.36 mol/L, or yet a volumetric fraction about 9.3 % per Liter assuming a density of 3.7.

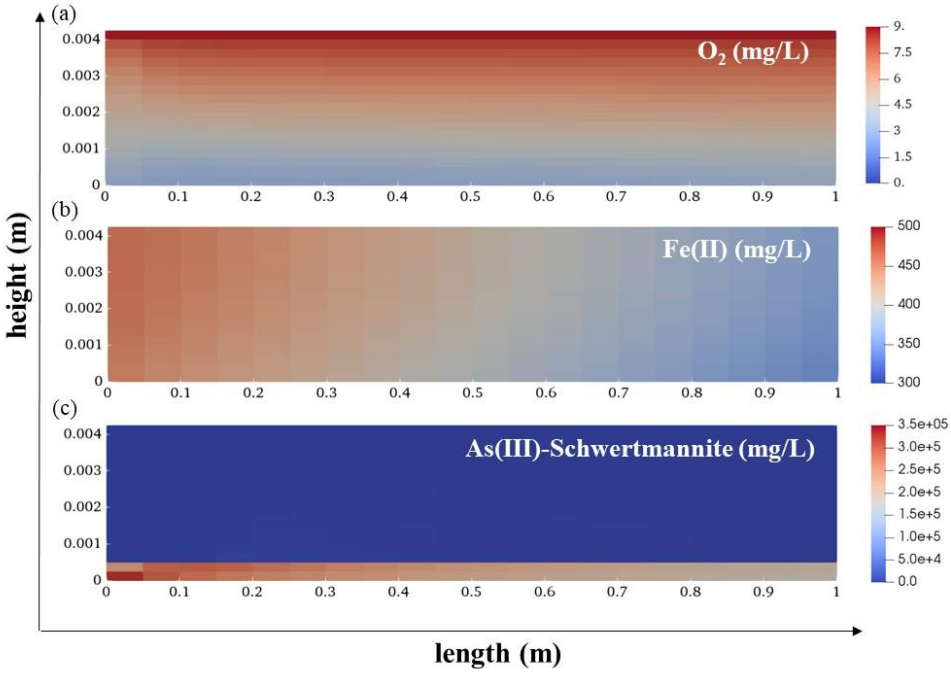

Figure 5. 2D longitudinal profiles showing (a) the concentration of dissolved O_2, (b) the concentration of aqueous Fe(II) and (c) the amount of As(III)-schwertmannite precipitation, obtained from the *FT4-3.9* model after 19 days of injection and a hydraulic retention time (HRT) around 100 min.

4. Discussion

4.1. Precipitation of As(III) and As(V) ferric minerals

The network of reactions that can be deduced from the modeling of the batch and flow-through experiments is given in **Fig. 6**. The evolution of the system is driven by the relatively fast oxidation of Fe(II) which is the rate-limiting step that promotes both precipitation of schwertmannite and amorphous ferric arsenate (AFA). However, the rather slow oxidation of As(III) prevents the formation of As(V)-AFA from the one hand, and favors the trapping of As(III) by schwertmannite precipitation from the other hand. This conceptual model is at least applicable to As(III)-rich AMD and a characteristic time

of a few weeks, as in the present case. The issue of kinetics of precipitation, the nature of As-bearing minerals and the effect of the hydraulic retention time are discussed in the next paragraphs of this section.

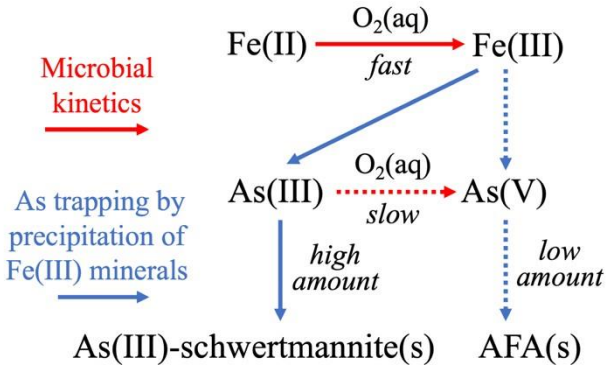

Figure 6. Schematic reaction network for the natural attenuation of arsenic and iron in the AMD of the Carnoulès mine deduced from the modeling of the batch and flow-through experiments (AFA stands for amorphous ferric arsenate).

Relatively scarce information concerning the rate of schwertmannite precipitation was found in the literature. It is worth noting that Fe(III) precipitation rate (expressed in $mol.L^{-1}.s^{-1}$) is 8 times faster than the rate of schwermannite precipitation (expressed in $mol.L^{-1}.s^{-1}$) due to the stoichiometry of schwermannite than corresponds to 8 moles of Fe per mole of mineral. Kirby et al. (1999) stated that the oxidation of Fe(II) was apparently the rate-limiting step in passive treatment of coal mine drainage. Sânchez-Espana et al. (2007) found that the rate of Fe(III) precipitation as schwermannite was 2 – 3 times lower than the respective rates of Fe(II) oxidation for AMD of two Spanish mines. Chen and Jiang (2012) reported high rates of As-bearing schwermannite precipitation in an acid mine drainage system in Taiwan. The authors stated than Fe(II) oxidation appeared to be the rate-determining reaction for Fe removal process in the creek section but not in the water fall section. Fernandez-Rojo et al. (2017) found that the Fe(II) oxidation rate was twice as fast as the total Fe precipitation rate. To the best of our knowledge, no AFA precipitation rate to compare with this study has been found in the literature.

For the sake of simplicity, As-mineral precipitation was modeled under thermodynamic equilibrium in this study. The good agreement between the modeling and experimental data in terms of precipitated masses (**Tables 4 and 5**) indicates that it was a reasonable approximation. But it is worth noting that this good agreement is partly due to the fitting of the formation constant of the As(III)-schwertmannite to the data. The fact that the solubility of this mineral is slightly above the solubility of pure schwertmannite (solubility diagram of **Fig. 2**) probably indicates that the kinetic delay in precipitation was included in the fitting. Whatsoever, the single fitted value of the formation constant of As(III)-schwertmannite was able to correctly simulate the whole set of batch and flow-through data (with the single exception of As(III) at the highest HRT in **Fig. 4c**).

Although the elements iron and arsenic are often encountered jointly in AMD, As(III)-ferric minerals are relatively uncommon. This is due to the usual predominance of As(V) upon As(III) in AMD water, which promotes the formation of As(V)-ferric minerals upon microbial Fe oxidation. However, As(III)-ferric minerals such as tooeleite or As(III)-schwertmannite are known from several AMD systems throughout the world (Mazlan et al. (2016) and reference therein). If specific conditions are met, in particular at high As(III) concentration in the AMD, these As(III) ferric minerals can form abundantly (Mazlan et al., 2016 ; Paikaray et al., 2011). In the specific case of the Carnoulès AMD, both field data and laboratory experiments showed that As(III) ferric minerals i.e. As(III)-schwertmannite or tooeleite are the major As-bearing solids forming upon microbial Fe(II) oxidation (Morin et al., 2003 ;

Egal et al., 2009). The formation of one or the other solid phase appeared to be controlled by the rate of Fe(II) oxidation ; higher Fe(II) oxidation rates favor the formation of As(III)-schwertmannite relative to tooeleite (Egal et al., 2009). The present study shows that fast Fe(II) oxidation rate also favors the formation of As(III)-schwertmannite relative to AFA due to the slower microbial As(III) oxidation.

The amount of secondary mineral precipitation varies depending on the hydraulic retention time (HRT) considered (**Fig. 4d**). The amounts of As(III)-schwertmannite and AFA precipitated (in mg) after 19 days of AMD water injection decreases when the HRT increases. The highest amounts of As-bearing precipitates are obtained for HRT values lower than 200 min. This may seem counter-intuitive from the point of view of oxidation kinetics. The higher the HRT, the more efficient the kinetics of Fe(II) oxidation. But it makes sense while considering the total amount of AMD water that have been injected in the bioreactor. Indeed, the lower the HRT, the higher the input of fresh AMD water after 19 days. The concentration of precipitated minerals per liter of injected solution can be calculated as the ratio of the mass given in **Fig. 4d** by the total number of liters injected during 19 days. The concentration of As(III)-schwertmannite is more than three times greater at high than at low HRT (303 mg L^{-1} and 91 mg L^{-1} of As(III)-schwertmannite at HRT of 600 min and 60 min, respectively). On the contrary, the concentration of AFA is similar at any HRT considered in this study (18 ± 2 mg per liter of injected solution). The fact that the concentration of Fe(III) in solution is higher at high HRT (**Fig. 4b**), both in the experiment and the modeling, is due to the slight decrease in pH that favors Fe(III) solubility (Larson et al., 2014 and solubility diagram of **Fig. 2**). Globally, it is worth noting that high HRTs favor As removal but also lead to higher concentrations of Fe(III) in solution.

4.2. Dissolved oxygen supply to the biofilm through the water thin film

Two *FT* models with inlet pH = 3.4 and different water height are presented in this section: model *FT4-3.4* with 4 mm water height and the *FT25-3.4* model with 25 mm water height (**Table 1**). The water height in the channel influences the transfer of the dissolved oxygen (O_2) from the atmosphere to the biofilm zone. As mentioned before, the dissolved O_2 profiles throughout the water film was the combination of two mass transfer processes in the model: the horizontal advective/dispersive flow imposed at the inlet of the channel as an input boundary condition, and the vertical mainly diffusive transfer from the air-solution interface to the bottom of the channel where oxidation reactions occur.

Fig. 7a, b shows the calculated and experimental vertical profiles of the dissolved O_2 concentration through the water column in the channel. Under abiotic conditions, the O_2 concentration profiles show no variation along the 4 mm water column and very little variation along the 25 mm water column. Given that no O_2 consumption occurs, the calculated dissolved O_2 concentration along the entire water column is very close to that in equilibrium with the atmosphere in both models from the one hand, in good agreement with the experimental measurement from the other hand. Under biotic conditions, the calculated O_2 concentration profile is close to the experimental one for 4 mm height. In the model, the linear profile corresponds to a diffusive steady state between two boundary conditions at fixed concentrations. The inlet concentration of dissolved oxygen O_2(aq) (4 mg L^{-1}, i.e. 5×10^{-4} equivalent of electron e^- per liter) is largely insufficient to fully oxidize the Fe(II) content of the AMD water (500 mg L^{-1}, i.e. 9×10^{-3} equivalent of electron e^- per liter of solution). Therefore, a significant input of oxygen from the atmospheric air was required in the model to sustain the oxidation reactions in the biofilm. In the model at 25 mm, the best match was obtained while increasing the scalar dispersivity from 5×10^{-5} and 7×10^{-4} m (**Table 1**) as to reach a linear diffusive/dispersive steady-state profile. That is to say that the dispersion in Eq. (2) varied from 1×10^{-9} to 3×10^{-8} m^2/s in the 4 mm cases, and from 2×10^{-8} to 4×10^{-7} m^2/s in the 25 mm cases (to be compared to the diffusion coefficient of 2×10^{-9} m^2/s). These dispersion values remain small due to the almost laminar flow in the channel that minimizes dispersion. The source of dispersion could be related to the channel walls or some roughness of the biofilm and its precipitates. Even so, the model did not match so well the O_2 concentration profiles measured for the 25 mm height. However, it is clear that the calculated O_2 concentration at proximity of the biofilm (about 1 mg L^{-1}) is

583 similar for the two heights and closed to the experimental data (about 2 mg L^{-1}) at 4 mm height given
584 the uncertainty of such O_2 analysis (there was no analysis in the biofilm zone for the 25 mm height
585 experiment). Eventually, it is worth emphasizing that the linear steady-state vertical profile of dissolved
586 O_2 concentration has been confirmed by another set of experiments performed with a 4 mm height water
587 film (data published in Fernandez-Rojo et al. (2017) but not modeled in this paper; see **Fig. SI-3**).

588 **Fig. 7c** shows the variation in aqueous Fe(II) concentration versus the hydraulic retention time
589 (HRT). Increasing HRT, the aqueous Fe(II) concentration (in mg L^{-1}) decreases sharply at 4 mm height
590 but remains fairly constant at 25 mm height. This trend occurs in both the model and the experiment. It
591 does not imply that Fe oxidation is much higher at 4 mm than 25 mm. The absolute amounts of Fe
592 oxidation (in mg), i.e. the concentration times the volume of solution, between the two configurations
593 only slightly differed from each other for all the HRTs. Hence, taking into account that microbial Fe(II)
594 oxidation is localized at the bottom of the channel, the amount of oxidation for a 4 mm water column
595 seems to be roughly comparable to that for a 25 mm water column. A similar process takes place for
596 As(III), with again a very good agreement between the calculated and experimental results. **Fig. 6d**
597 shows that this agreement remains at high HRTs where the As(III) concentration becomes very low.

598 Globally, the local activities inside the bacterial biofilm seems to be similar for both water heights.
599 Therefore, they are not significantly limited by the O_2 supply from both the inlet solution and the
600 atmosphere. But the scavenging of As(III) and Fe(II) in terms of concentration decrease is not efficient
601 enough in the case of the 25 mm height.

602 A sheet-flow regime is assumed to allow for efficient diffusion of oxygen from atmospheric air to the
603 water film (e.g. Gouin et al., 2013). Several authors have evidenced a greater Fe(II) concentration
604 decrease in some sections of AMD streams characterized by a shallow sheet-like flow above terraced
605 iron mound as opposed to other sections characterized by deep water pools (Chen and Jiang, 2012;
606 Brown et al., 2011). Such a greater Fe(II) oxidation efficiency was generally attributed to improved
607 aeration generated by turbulent hydrodynamic conditions (Chen and Jiang, 2012). In the present study
608 there was no turbulent flow, and similar O_2 concentrations, around 1 mg L^{-1}, were determined in the
609 biofilm zone, both at 4 mm and 25 mm water height. Thus, greater Fe(II) concentration decrease at 4
610 mm was attributed to the limitation of the Fe(II) oxidation activity to the biofilm zone near the channel
611 bottom. This active zone represented a smaller fraction of the whole water volume in the channel as the
612 water height increased. Thus, decreasing Fe(II) concentration in this zone did not affect the whole water
613 chemistry significantly. A major consequence is the need for a higher biofilm surface area per water
614 volume unit, in view of the application of the natural attenuation process to AMD treatment.

615

616

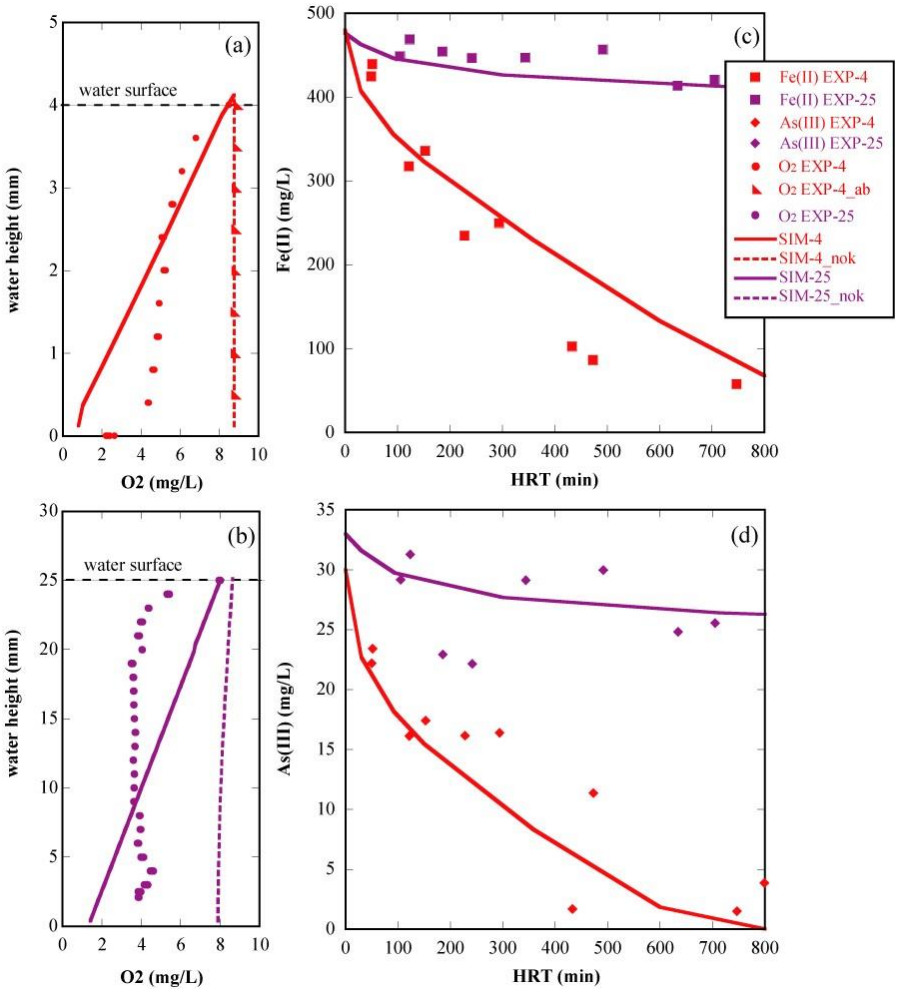

Figure 7. Dissolved O_2 concentration profiles for a 4 mm height (a) and 25 mm-height (b) of the water film; variation in Fe(II) (c) and As(III) (d) concentration versus the hydraulic retention time (HRT) for both heights; experimental data from Fernandez-Rojo et al. (2017); the dotted lines indicate modeling results under abiotic conditions without any oxidation kinetics (with the label *nok*).

4.3. Effects of biofilm bacteria concentration and pH on the oxidation rates

As specified in **Section 2.4,** several authors (Pesic et al., 1989; Kirby et al., 1999; Sheng et al., 2017) implemented a four-order reaction with the additional dependency of the kinetic rate upon the concentration of proton and Fe(II)-oxidizing bacteria. In the present study, it was not obvious to quantify the proportion of active bacteria within the microbial population of the biofilm from the one hand, and the types of bacteria in the biofilm evolved with the pH from the other hand. Like Asta et al. (2010), the microbial Fe(II) oxidation was, therefore, modeled by a simplified second-order kinetic rate law depending on the concentrations of the substrates Fe(II) and dissolved O_2. This approach correctly reproduced most of the batch and flow-through experimental data.

The modeling results showed that rate constant was at least two orders of magnitude higher in the biofilm of flow-through experiments than in the planktonic bacteria of the batch experiment (*e.g.*, k_{Fe} = 2.7×10^{-2} L mol^{-1} s^{-1} in the *B* model and k_{Fe} = 5 L mol^{-1} s^{-1} in the *FT4-3.9* model). This factor is well correlated to the two orders of magnitude higher concentration of Fe(II)-oxidizing bacteria measured in the flow-through experiments compared to that measured in the batch experiment (about 10^7 and 10^5 cells mL^{-1}, respectively). This trend can only be an estimation since the fraction of bacteria in the biofilm that are really active in the oxidation of Fe(II) is not known. Whatsoever, the present rate constant k_{Fe} values are in line with the k_{Fe} values obtained under very similar AMD conditions. Using a first order

kinetics formulation for microbial Fe(II) oxidation, Larson et al. (2014) obtained in batch experiments a rate constant about 4×10^{-4} s^{-1} with a population of 10^7 cells mL^{-1}. A rate constant k_{Fe} (Eq. 5) of about 4 L mol^{-1} s^{-1} can be derived by considering an $[O_2(aq)]$ of 10^{-4} mol L^{-1}. It is comparable to the present data in flow-through experiments (k_{Fe} = 5 L mol^{-1} s^{-1} with 10^7 cells mL^{-1}). Similarly, and considering that the authors used a first order kinetic expression, a rate constant k_{Fe} of about 10^{-1} L mol^{-1} s^{-1} can be derived using the data of Xiong et al., (2008) for microbial Fe(II) oxidation in a system containing 10^6 cells mL^{-1} (Chen and Jiang 2012). The reactive transport modelling performed by Asta et al (2010) gave k_{Fe} values within the same order of magnitude as Xiong et al., (2008), after the translation of the partial pressure of O_2 in terms of dissolved O_2 in mol L^{-1}, even if no detailed information about the concentration of bacteria involved in the process was provided in their study.

In **Table 2**, the rate constant of Fe(II) oxidation of the *FT4-3.9* model (k_{Fe} = 5 L mol^{-1} s^{-1}) was fitted on the experimental data of Fernandez-Rojo et al. (2018). In the pH range 2.5 – 4, the kinetic rate constants of models were extrapolated from the fitted value based on the linear dependency with the proton concentration ($[H^+]$) of the input solution (**Eq. 6** and Kirby et al., 1999; Larson et al., 2014). **Fig. 8** shows the calculated variation of Fe(II) concentration versus the hydraulic retention time (HRT) according to this assumption. The lower the pH, the higher the rate of oxidation, as globally expected from the linear dependency with $[H^+]$. However, the discrepancy between the modeling and experimental results increases as the acidity of the input solution increases. The *FT4-3.1* model (with inlet pH = 3.1) clearly underestimates the experimental data of Fe(II) oxidation for HRT beyond 100 min. The reason that could explain the disagreement obtained at low pH and long HRT is probably related to the type of bacteria involved in the process. Indeed, the microbial analysis performed in these experiments revealed that the bacterial community structure in the inlet water at pH 3.1 and 3.4 differed widely (Fernandez-Rojo et al., 2017). The type of Fe(II)-oxidizing bacteria also varied depending on the hydraulic retention time (Fernandez-Rojo et al. 2018). Increasing the HRT, the most abundant bacteria changed from *Gallionella* to *Ferrovum*. The fact that *Ferrovum* was reported to achieve the fastest iron oxidation rates among the most common Fe(II)-oxidizing bacteria (Johnson et al., 2012; Jones et al., 2015) supports the high Fe(II) oxidation observed at low pH and long HRT. In other words, this is not only the amount of bacteria that controls the kinetics of AMD attenuation but also the types of bacteria present in the biofilm.

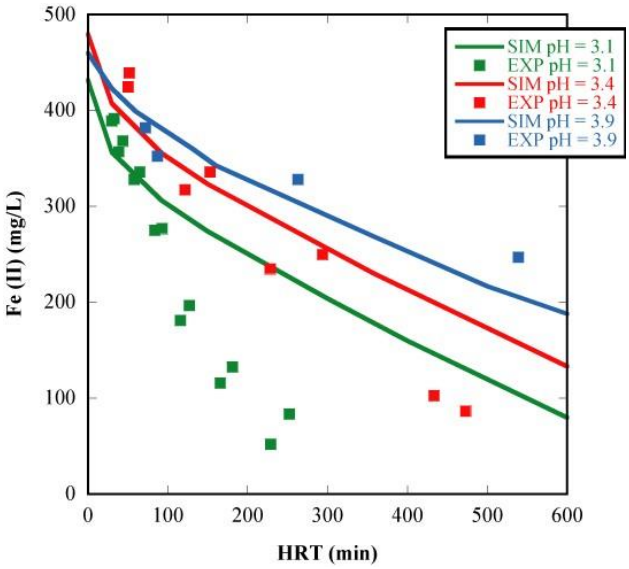

Figure 8. Calculated Fe(II) concentration versus the hydraulic retention time (HRT) obtained from the *FT4-3.9*, *FT4-3.4* and *FT4-3.1* models (**Table 2**); the bleu squares correspond to the experiments *c1–c4* of Fernandez-Rojo et al. (2018); the red and green squares correspond to *Exp2(4mm)* and *Exp1(OA)*

of Fernandez-Rojo et al. (2017), respectively. It is worth mentioning that the relatively poor agreement at high HRT and low pH (green curve in Fig 8). The pH did not change significantly (from 3.1 to 2.9) in those experiments and could not significantly affect the kinetics. The disagreement would rather illustrate the lack of consideration of bacterial community structure changes in the model.

The microbial oxidation of As(III) was slow in the present batch and flow-through experiments conducted at 20 °C. Previous investigations showed that bacterial strains isolated from the Carnoulès AMD and belonging to the *Thiomonas* genera promoted the oxidation of As(III) (Casiot et al., 2003 ; Bruneel et al., 2003). The long-term monitoring of this AMD showed that several *Thiomonas* strains are present in the sediments at different time periods and express an arsenite oxidase enzyme (Hovasse et al., 2016). In agreement with these previous findings, the *aioA* marker gene coding for an enzyme responsible for microbial As(III) oxidation has been detected in the batch and flow-through experiments under study (Fernandez-Rojo et al., 2017, 2018 ; Tardy et al., 2018). However, arsenite-oxidizing bacteria are minor representatives of the bacterial community in the biofilm. The *Thiomonas* genus represented only 2-3% of the whole community (Fernandez-Rojo et al., 2018). Therefore, the microbial As-oxidizing activity was not favored in the conditions of the present experiments. It is difficult to conclude on the effects of bacteria concentration and pH upon the kinetics of As(III) oxidation. The analysis of such dependencies was masked by the dominant and fast processes of Fe(II) oxidation and the precipitation of As(III)-schwertmannite. The rate constant k_{As} fitted on the batch experiment was very low, i.e. four orders of magnitude smaller than the rate constant k_{Fe} (**Table 2**). Tardy et al. (2018) showed that the microbial oxidation of As(III) in the Carnoulès AMD became only efficient at 35 °C in their batch experiments. A slight microbial As(III) oxidation (≤ 10 %) took place in the flow-through experiments at 20 °C. The fitted rate constant k_{As} was at least one order of magnitude smaller than the rate constant k_{Fe}. Using a first order kinetics formulation for microbial oxidation of As(III), Wan et al. (2010) obtained a rate constant of about 5×10^{-4} s^{-1} in fixed-bed bioreactor inoculated with As-oxidizing bacteria of the same genus (*Thiomonas*) than in the Carnoulès AMD. A rate constant k_{As} (Eq. 8) in the order of 5 L mol^{-1} s^{-1} can be derived by considering an $[O_2(aq)]$ of 10^{-4} mol L^{-1}. It is roughly ten times higher than the present rate constant, nevertheless it remains difficult to precisely compare the bacteria concentrations between these two studies.

5. Concluding remarks for in site passive treatment of AMD

The model developed in this study gave an integrated view of geochemical and transport processes involved in natural attenuation in high-As AMD. It was able to correctly simulate the data from both batch and flow-through experiments using a limited number of chemical reactions and fitting parameters. The global reaction presents a positive feedback loop. The progressive oxidation of Fe(II) leads to the precipitation of schwertmannite. This precipitation progressively decreases the pH. This decrease of pH enhances the kinetics of Fe(II) oxidation. The increase of rate constant values for Fe oxidation from batch to flow-through experiments at an initial pH of 3.5 – 4.0 was consistent with the bacterial concentration increase due to the presence of a biofilm. At the most acidic initial values of 3.1, the model failed in reproducing experimental data at the highest HRT. This suggests that the change to bacterial community composition, which is not considered in the modeling, exerts a control on Fe oxidation rate, besides bacterial concentration and pH.

Modeling of oxygen concentration profiles in flow-through experiments revealed that the biofilm activity was not limited by the oxygen supply in both the 4 mm and 25 mm heights. Conversely, the surface of biofilm per water volume was clearly a limiting factor in the 25 mm height. This is an important issue for future design of a passive treatment step for As-rich AMD. A filling porous material should be provided to improve the biofilm surface and, consequently, the Fe oxidation efficiency. High HRTs favored As removal but also led to higher concentrations of Fe(III) in solution. The latter is not so suitable to feed lime neutralization units in chains of AMD treatment, since pH neutralization may generate clogging by Fe(III)-hydroxide precipitation. The trend of curves representing the amount of

As-bearing phases precipitated as a function of HRT revealed that the highest amount was obtained for HRT lower than 200 min. This trend may guide the choice of operating conditions most suitable for future treatment implementation. The highest amount of precipitate formed at lowest HRT may be preferred to As removal performance when considering the present treatment as a first step of a whole AMD treatment scheme.

6. Acknowledgements

This work was supported by the Agence de l'Environnement et de la Maîtrise de l'Energie (ADEME) [APR-GESIPOL-2017-COMPAs]. It benefited from previous experimental and observation data acquired during previous projects funded by ANR [IngECOST-DMA ANR-13-ECOT-0009], OSU OREME [Pollumine Observation System] and University of Montpellier [PhD fellowship of Lidia Fernandez-Rojo, GAIA Doctoral School, 2014-2017]. The relevant comments and suggestions of the reviewers are also gratefully acknowledged.

7. References

Ahoranta, S. H., Kokko, M. E., Papirio, S., Özkaya, B., Puhakka, J. A. (2016). Arsenic removal from acidic solutions with biogenic ferric precipitates. J. Hazard. Mater. 306, 124–132. https://doi.org/10.1016/j.jhazmat.2015.12.012.

Asta, M.P., Ayora, C., Acero, P., Cama, J. (2010). Field rates for natural attenuation of arsenic in Tinto Santa Rosa acid mine drainage (SW Spain). J. Hazard. Mater. 177, 1102-1111. https://doi.org/10.1016/j.jhazmat.2010.01.034.

Balistrieri, L. S., Box, S. E., Tonkin, J. W. (2003). Modeling precipitation and sorption of elements during mixing of river water and porewater in the Coeur d'Alene River basin. Environmental Science and Technology, 37(20), 4694–4701. https://doi.org/10.1021/es0303283.

Berger, A. C., Bethke, C. M., Krumhansl, J. L. (2000). A process model of natural attenuation in drainage from a historic mining district. Applied Geochemistry, 15(5), 655–666. https://doi.org/10.1016/S0883-2927(99)00074-8.

Bigham, J.M., Schwertmann, U., Traina, S.J., Winland, R.L., Wolf, M. (1996). Schwertmannite and the chemical modeling of iron in acid sulfate waters. Geochimica et Cosmochimica Acta 60, 2111-2121. https://doi.org/10.1016/0016-7037(96)00091-9.

Blanc, P., Lassin, A., Piantone, P., Azaroual, M., Jacquemet, N., Fabbri, A., Gaucher, E.C. (2012). Thermoddem: a geochemical database focused on low temperature water/rock interactions and waste materials. Applied Geochemistry 27, 2107–2116.

Brown, J.F., Jones, D.S., Mills, D.B., Macalady, J.L., Burgos, W.D. (2011). Application of a depositional facies model to an acid mine drainage site. Appl. Environ. Microbiol. 77, 545–554. https://doi.org/10.1128/AEM.01550-10.

Bruneel, O., Personné, J.C., Casiot, C., Leblanc, M., Elbaz-Poulichet, F., Le Flèche, A. and Grimont, P.A.D. (2003). *Thiomonas* sp. mediated arsenic oxidation in acid mine drainage (Carnoulès creek, France), Journal of Applied Microbiology, 95(3), 492-499. doi:10.1046/j.1365-2672.2003.02004.x.

Burton, E.D., Bush, R.T., Johnston, S.G., Watling, K.M., Hocking, R.K., Sullivan, L.A., Parker, G.K. (2009). Sorption of Arsenic(V) and Arsenic(III) to schwertmannite. Environ. Sci. Technol. 43, 9202–9207. https://doi.org/10.1021/es902461x.

Casiot, C., Morin, G., Juillot, F., Bruneel, O., Personné, J. C., Leblanc, M., Duquesne, K., Bonnefoy, V., Elbaz-Poulichet, F. (2003). Bacterial immobilization and oxidation of arsenic in acid mine drainage (Carnoulès creek, France). Water Research, 37(12), 2929–2936. https://doi.org/10.1016/S0043-1354(03)00080-0.

Chai, L., Yue, M., Yang, J., Wang, Q., Li, Q., Liu, H. (2016). Formation of tooeleite and the role of direct removal of As(III) from high-arsenic acid wastewater. J. Hazard. Mater. 320, 620–627. doi:10.1016/j.jhazmat.2016.07.069.

Chen, C., Jiang, W. (2012). Influence of waterfall aeration and seasonal temperature variation on the iron and arsenic attenuation rates in an acid mine drainage system. Appl. Geochem. 27, 1966-1978. https://doi.org/10.1016/j.apgeochem.2012.06.003.

Cheng, H., Hu, Y., Luo, J., Xu, B., Zhao, J. (2009). Geochemical processes controlling fate and transport of arsenic in acid mine drainage (AMD) and natural systems. J. Hazard. Mater., 165(1–3), 13–26. https://doi.org/10.1016/j.jhazmat.2008.10.070.

Diz, B. H. R., Novak, J. T. (1999). Modeling biooxidation of iron in packed-bed reactor. J. Environ. Eng. 125, 109–116.

Drahota, P., Filippi, M. (2009). Secondary arsenic minerals in the environment: A review. Environ. Int. 35, 1243–1255. doi:10.1016/j.envint.2009.07.004.

Egal, M., Casiot, C., Morin, G., Parmentier, M., Bruneel, O., Lebrun, S., Elbaz-Poulichet, F. (2009). Kinetic control on the formation of tooeleite, schwertmannite and jarosite by Acidithiobacillus ferrooxidans strains in an As(III)-rich acid mine water. Chem. Geol. 265, 432–441. https://doi.org/10.1016/j.chemgeo.2009.05.008.

Fernandez-Rojo, L., Casiot, C., Laroche, E., Tardy, V., Bruneel, O., Delpoux, S., Desoeuvre, A., Grapin, G., Savignac, J., Boisson, J., Morin, G., Battaglia-Brunet, F., Joulian, C., Héry, M. (2019). A field-pilot for passive bioremediation of As-rich acid mine drainage. J. of Environ. Manag., 232(November 2018), 910–918. https://doi.org/10.1016/j.jenvman.2018.11.116.

Fernandez-Rojo, L., Casiot, C., Tardy, V., Laroche, E., Le Pape, P., Morin, G., Joulian, C., Battaglia-Brunet, F., Braungardt, C., Desoeuvre, A., Delpoux, S., Boisson, J., Héry, M. (2018). Hydraulic retention time affects bacterial community structure in an As-rich acid mine drainage (AMD) biotreatment process. Appl. Microbiol. Biotechnol. 102, 9803–9813. https://doi.org/10.1007/s00253-018-9290-0.

Fernandez-Rojo, L., Héry, M., Le Pape, P., Braungardt, C., Desoeuvre, A., Torres, E., Tardy, V., Resongles, E., Laroche, E., Delpoux, S., Joulian, C., Battaglia-Brunet, F., Boisson, J., Grapin, G., Morin, G., Casiot, C. (2017). Biological attenuation of arsenic and iron in a continuous flow bioreactor treating acid mine drainage (AMD). Water Res. 123, 594–606. https://doi.org/10.1016/j.watres.2017.06.059.

Gouin, M., Saracusa, E., Clemons, C. B., Senko, J., Kreider, K. L., Young, G. W. (2013). A mathematical model of a passive scheme for acid mine drainage remediation. GEM - International Journal on Geomathematics, 4(1), 27–53. https://doi.org/10.1007/s13137-012-0044-3.

Hovasse, A., Bruneel, O., Casiot, C., Desoeuvre, A., Farasin, J., Hery, M., Van Dorsselaer, A., Carapito, C. and Arsène-Ploetze, F. (2016). Spatio-Temporal Detection of the *Thiomonas* Population and the *Thiomonas* Arsenite Oxidase Involved in Natural Arsenite Attenuation Processes in the Carnoulès Acid Mine Drainage. Front. Cell Dev. Biol., 4:3. doi: 10.3389/fcell.2016.00003.

Indraratna, B. Pathirage, P.U, Kerry Rowe, R., Banasiak, L. (2014). Coupled hydro-geochemical modelling of a permeable reactive barrier for treating acidic groundwater. Comput. Geotechn. 55, 429–439, https://doi.org/10.1016/j.compgeo.2013.09.025.

Johnson, D. B., Hallberg, K. B. (2005). Acid mine drainage remediation options: A review. Sci. Total Environ., 338(1-2 SPEC. ISS.), 3–14. https://doi.org/10.1016/j.scitotenv.2004.09.002.

Johnson, D.B., Kanao, T., Hedrich, S. (2012). Redox transformations of iron at extremely low pH: fundamental and applied aspects. Front. Microbiol. 3, 96. https://doi.org/10.3389/fmicb.2012.00096.

Jones, D.S., Kohl, C., Grettenberger, C., Larson, L.N., Burgos, W.D., Macalady, J.L. (2015). Geochemical niches of iron-oxidizing acidophiles in acidic coal mine drainage. Appl. Environ. Microbiol. 81, 1242-1250. https://doi.org/10.1128/AEM.02919-14.

Karamanev, D.G., Nikolov, L.N. (1988). Influence of some physicochemical parameters on bacterial activity of biofilm: Ferrous iron oxidation by Thiobacillus ferrooxidans. Biotechnology and Bioengineering 31, 295-299. https://doi.org/10.1002/bit.260310403.

Kirby, C.S., Thomas, H.M., Southam, G., Donald, R. (1999). Relative contributions of abiotic and biological factors in Fe(II) oxidation in mine drainage. Appl. Geochem. 14, 511-530. https://doi.org/10.1016/S0883-2927(98)00071-7.

816 Langmuir, D., Mahoney, J., Rowson, J. (2006). Solubility products of amorphous ferric arsenate and crystalline
817 scorodite ($FeAsO4{\cdot}2H_2O$) and their application to arsenic behavior in buried mine tailings. Geochim.
818 Cosmochim. Acta 70, 2942–2956. https://doi.org/10.1016/j.gca.2006.03.006.

819 Larson, L.N., Sánchez-España, J., Kaley, B., Sheng, Y., Bibby, K., Burgos, W.D (2014). Thermodynamic controls
820 on the kinetics of microbial low-pH Fe(II) oxidation. Environ. Sci. Technol. 48, 9246–9254.
821 https://doi.org/10.1021/es501322d.

822 Liao, Y., Liang, J., Zhou, L. (2011). Adsorptive removal of As(III) by biogenic schwertmannite from simulated
823 As-contaminated groundwater. Chemosphere 83, 295–301.

824 Maillot, F., Morin, G., Juillot, F., Bruneel, O., Casiot, C., Ona-Nguema, G., Wang, Y., Lebrun, S., Aubry, E.,
825 Vlaic, G., Brown, G.E. (2013). Structure and reactivity of As(III)- and As(V)-rich schwertmannites and
826 amorphous ferric arsenate sulfate from the Carnoulès acid mine drainage, France: Comparison with biotic
827 and abiotic model compounds and implications for As remediation. Geochim. Cosmochim. Acta 104, 310–
828 329. https://doi.org/10.1016/j.gca.2012.11.016.

829 Mayer, K. U., Benner, S. G., Blowes, D. W. (2006). Process-based reactive transport modeling of a permeable
830 reactive barrier for the treatment of mine drainage. J. Contam. Hydr. 85, 195–211.

831 Majzlan, J., Dachs, E., Benisek, A., Bender Koch, C., Bolanz, R., Göttlicher, J., Steininger, R. (2016).
832 Thermodynamic properties of tooeleite, $Fe_6^{3+}(As^{3+}O_3)_4(SO_4)(OH)_4{\cdot}4H_2O$. Chemie der Erde 76, 419–428.
833 http://dx.doi.org/10.1016/j.chemer.2016.05.001.

834 Morin, G., Juillot, F., Casiot, C., Bruneel, O., Personné, J. C., Elbaz-Poulichet, F., Leblanc, M., Ildefonse, P.,
835 Calas, G. (2003). Bacterial formation of tooeleite and Mixed Arsenic(III) or Arsenic(V) - Iron(III) gels in
836 the carnoulès acid mine drainage, France. A XANES, XRD, and SEM study. Environ. Sci. Technol., 37(9),
837 1705–1712. https://doi.org/10.1021/es025688p.

838 Noike T., Nakamura, K., Matsumoto, J. (1988). Oxidation of ferrous iron by acidophilic iron-oxidizing bacteria
839 from a stream receiving acid mine drainage. Water Research 17, 21-27. https://doi.org/10.1016/0043-
840 1354(83)90282-8.

841 Paikaray, S., Göttlicher, J., Peiffer, S. (2011). Removal of As(III) from acidic waters using schwertmannite:
842 Surface speciation and effect of synthesis pathway. Chemical Geology 283, 134–142.

843 Paikaray, S. (2015). Arsenic Geochemistry of Acid Mine Drainage. Mine Water Environ., 34(2), 181–196.
844 https://doi.org/10.1007/s10230-014-0286-4.

845 Paikaray, S., Peiffer, S. (2012). Biotic and Abiotic Schwertmannites as Scavengers for As(III): Mechanisms and
846 Effects. Water Air Soil Pollut 223, 2933–2942.

847 Paikaray, S., Essilfie-Dughan, J., Göttlicher, J., Pollok, K., Peiffer, S. (2014). Redox stability of As(III) on
848 schwertmannite surfaces. J. Hazard. Mater. 265, 208–216.

849 Paktunc, D., Bruggeman, K. (2010). Solubility of nanocrystalline scorodite and amorphous ferric arsenate:
850 Implications for stabilization of arsenic in mine wastes. Appl. Geochem. 25, 674–683.
851 https://doi.org/10.1016/j.apgeochem.2010.01.021.

852 Park, J.H., Han, Y.S., Ahn, J.S. (2016). Comparison of arsenic co-precipitation and adsorption by iron minerals
853 and the mechanism of arsenic natural attenuation in a mine stream. Water Res. 106, 295–303,
854 https://doi.org/10.1016/j.watres.2016.10.006.

855 Pesic, B., Oliver, D.J., Wichlacz, P. (1989). An electrochemical method of measuring the oxidation rate of ferrous
856 to ferric iron with oxygen in the presence of *Thiobacillus ferrooxidans.* Biotechnol. Bioeng. 33, 428-439.
857 https://doi.org/10.1002/bit.260330408.

858 Regenspurg, S., Peiffer, S. (2005). Arsenate and chromate incorporation in schwertmannite. Appl. Geochem. 20,
859 1226–1239.

860 Sánchez España, J., López Pamo, E., Santofimia Pastor, E. (2007). The oxidation of ferrous iron in acidic mine
861 effluents from the Iberian Pyrite Belt (Odiel Basin, Huelva, Spain): Field and laboratory rates. J.
862 Geochemical Explor. 92, 120–132. https://doi.org/10.1016/j.gexplo.2006.08.010.

863 Sánchez-España, J., Yusta, I., Diez-Ercilla, M. (2011). Schwertmannite and hydrobasaluminite: A re-evaluation

of their solubility and control on the iron and aluminium concentration in acidic pit lakes. Appl. Geochem. 26, 1752-1774. https://doi.org/10.1016/j.apgeochem.2011.06.020.

Savić, D. S., Veljković, V. B., Lazić, M. L., Vrvić, M. M., Vučetić, J. I. (1998). Effects of the oxygen transfer rate on ferrous iron oxidation by Thiobacillus ferrooxidans. Enzyme Microb. Technol., 23(7–8), 427–431. https://doi.org/10.1016/S0141-0229(98)00071-4.

Sheng, Y., Kaley, B., Bibby, K., Grettenberger, C., Macalady, J. L., Burgos, W. D. (2017). Bioreactors for low-pH iron(II) oxidation remove considerable amounts of total iron. RSC Advances, 7, 35962–35972. https://doi.org/10.1039/C7RA03717A.

Tardy, V., Casiot, C., Fernandez-Rojo, L., Resongles, E., Desoeuvre, A., Joulian, C., Battaglia-Brunet, F., Héry, M. (2018). Temperature and nutrients as drivers of microbially mediated arsenic oxidation and removal from acid mine drainage. Appl. Microbiol. Biotechnol. 102, 2413–2424. https://doi.org/10.1007/s00253-017-8716-4.

Tonkin, J. W., Balistrieri, L. S., Murray, J. W. (2002). Modeling metal removal onto natural particles formed during mixing of acid rock drainage with ambient surface water. Environ. Sci. Technol., 36(3), 484–492. https://doi.org/10.1021/es0109085.

van der Lee, J., De Windt, L., Lagneau, V., Goblet, P. (2003). Module-oriented modeling of reactive transport with HYTEC. Comput Geosci 29, 265–275.

Wan, J., Klein, J., Simon, S., Joulian, C., Dictor, M.C., Deluchat, V., Dagot, C. (2010). AsIII oxidation by Thiomonas arsenivorans in up-flow fixed-bed reactors coupled to As sequestration onto zero-valent iron-coated sand. Water Res. 44, 5098–5108.

Williams, M. (2001). Arsenic in mine waters: International study. Environ. Geol., 40(3), 267–278. https://doi.org/10.1007/s002540000162.

Xiong, H., Liao, Y., Zhou, L. (2008). Influence of chloride and sulfate on formation of akaganéite and schwertmannite through ferrous biooxidation by Acidithiobacillus Ferrooxidans cells. Environ. Sci. Technol. 42, 23, 8681-8686. https://doi.org/10.1021/es801646j.

Yavari, M., Ebrahimi, S., Aghazadeh, V., Ghashghaee, M. (2019). Kinetics of different bioreactor systems with *Acidithiobacillus ferrooxidans* for ferrous iron oxidation. Reac Kinet Mech Cat 128, 611–627. https://doi.org/10.1007/s11144-019-01660-3.

Yu, J.Y, Heo, B., Choi, I.K., Cho, J.P., Chang, H.W. (1999). Apparent solubilities of schwertmannite and ferrihydrite in natural stream waters polluted by mine drainage. Geochimica et Cosmochimica Acta 63, 3407-3416. https://doi.org/10.1016/S0016-7037(99)00261-6.